Published in final edited form as:
Sci Signal. ; 8(408): ra131. doi:10.1126/scisignal.aab1901.

A calcium-accumulating region, CAR, in the channel Orai1 enhances Ca^{2+} permeation and SOCE-induced gene transcription

Irene Frischauf[#1], **Vasilina Zayats**[#2,3], **Michael Deix**[1], **Anna Hochreiter**[1,4], **Isaac Jardin Polo**[1], **Martin Muik**[1], **Barbara Lackner**[1], **Barbora Svobodová**[1,5], **Teresa Pammer**[1], **Monika Litviňuková**[1], **Amrutha Arumbakam Sridhar**[1], **Isabella Derler**[1], **Ivan Bogeski**[6], **Christoph Romanin**[1], **Rüdiger H. Ettrich**[2,3], and **Rainer Schindl**[1]

[1]Institute of Biophysics, JKU Life Science Center, Johannes Kepler University Linz, Gruberstrasse 40, 4020 Linz, Austria

[2]Center for Nanobiology and Structural Biology, Institute of Microbiology, Academy of Sciences of the Czech Republic, Zamek 136, CZ-373 33, Nove Hrady, Czech Republic

[3]Faculty of Sciences, University of South Bohemia, Zamek 136, CZ-373 33, Nove Hrady, Czech Republic

[4]Institute for Experimental and Clinical Cell Therapy, Paracelsus Medical University, A-5020 Salzburg, Austria

[5]Institute for Biophysics of Medical University Graz, A-8010, Graz, Austria

[6]Department of Biophysics, School of Medicine, University of Saarland, D-66421 Homburg, Germany

[#] These authors contributed equally to this work.

Abstract

The Ca^{2+} release-activated Ca^{2+} channel mediates Ca^{2+} influx in a plethora of cell types, thereby controlling diverse cellular functions. The channel complex is composed of STIM1, an endoplasmic reticulum Ca^{2+} sensing protein and Orai1, a plasma membrane Ca^{2+} channel. Channels composed of STIM1 and Orai1 mediate Ca^{2+} influx even at low extracellular Ca^{2+} concentrations. We investigated if the activity of Orai1 adapted to different environmental Ca^{2+} concentrations. We used homology modelling and molecular dynamics simulations to predict the presence of an extracellular Ca^{2+}-accumulating region (CAR) at the pore entrance of Orai1. Furthermore, simulations of Orai1 proteins with mutations in CAR, along with live-cell experiments, or simulations and electrophysiological recordings of the channel with transient,

Correspondence should be addressed to Rainer Schindl: rainer.schindl@jku.at and Rüdiger H. Ettrich: ettrich@nh.cas.cz.

Contribution: R.S., I.F. R.H.E. conceived the ideas, directed the work and designed the study. I.F. designed and generated all the plasmid constructs. R.S. and B.L. performed patch-clamp experiments. M.M., I.J.P., M.L., I.B. and R.S. performed fluorescence experiments. V.Z. and R.H.E. performed computational modelling and molecular dynamics simulations. I.F., M.D., A.H., B.S, T.P., A.A.S. prepared membranes and crosslinking experiments. I.F, V.Z.,I.J.P., M.M., M.L., I.D., I.B.,C.R.,R.H.E and R.S. analyzed data, with input from the other authors. R.S. and R.H.E. wrote the manuscript.

Competing financial interests: All authors declare no competing financial interests.

Field codes: BIOCHEM, CELL BIOL

SPi: Specify HEK293 throughout. There should be no occurrences of HEK.

Europe PMC Funders Author Manuscripts

electrostatic loop3 interacting with loop1 (the site of CAR), determined that CAR enhanced Ca^{2+} permeation most efficiently at low external Ca^{2+} concentrations. Consistent with these results, cells expressing Orai1 CAR mutants exhibited impaired gene expression stimulated by the Ca^{2+}-activated transcription factor NFAT. We propose that the Orai1 channel architecture with a close proximity of CAR to the selectivity filter, which enables Ca^{2+}-selective ion permeation, enhances the local extracellular Ca^{2+} concentration to maintain Ca^{2+}-dependent gene regulation even in environments with relatively low Ca^{2+}concentrations.

Introduction

The channel complex STIM/Orai, which is composed of a member of the family of intracellular calcium-sensing proteins called stromal interaction molecules (STIMs) and a member of the Orai1 family of calcium-conducting channels, provides a route of Ca^{2+} influx for physiological Ca^{2+} signaling in immune cells, as well as in various other tissues, such as skin and muscle (1–4). Understanding this Ca^{2+}-entry pathway also has important pathophysiological implications in such diseases as autoimmunity, atherosclerosis, and cancer (5–7). The STIM/Orai channels function in multiple distinct environmental Ca^{2+} concentrations. Whereas Ca^{2+} concentrations range from 1-2 mM in the blood or lymph system, those in the basal epidermal layer are only 0.2 mM (8, 9). These distinct Ca^{2+} concentrations impact the driving force for Ca^{2+} influx. The amplitude, frequency, and duration of Ca^{2+} signals regulate the activation of specific transcription factors, including nuclear factor of activated T cells (NFAT) (10, 11). Thus, NFAT signaling depends on the extracellular Ca^{2+} concentration.

Structural insight into the Orai channel from *Drosophila melanogaster* depicts a hexameric assembly of Orai subunits arranged around a central ion pore (12). The first transmembrane (TM1) helix from each of the six subunits composes the funnel-structured pore that extends into the cytosol, and this pore is surrounded by TM2, TM3, and TM4. The pore-forming TM1 helices determine both gating and ion permeation (13–18). Here, we investigated the properties of the region surrounding the pore entrance by homology modelling, molecular dynamics simulations, and functional live-cell experiments and identified a calcium-accumulating region (CAR) that enhances Ca^{2+} permeation under conditions of low extracellular Ca^{2+} concentration. Experiments with mutant proteins expressed in cells also expressing an NFAT-dependent reporter revealed that CAR contributed to store-operated Ca^{2+} entry (SOCE)-mediated transcription. Our results indicated that CAR, in the context of the narrow pore that is unique to Ca^{2+} channels of the Orai family, enabled highly Ca^{2+}-selective influx necessary for NFAT-dependent gene transcription in mast cells and melanoma cells.

Results

CAR in Orai1 is predicted to increase the local concentration of Ca^{2+} near the selectivity filter

To provide insight into Ca^{2+} sensing and permeation, we initially took advantage of the high sequence identity of the crystallized *Drosophila melanogaster* Orai channel (12) of 63% to

Europe PMC Funders Author Manuscripts

human Orai1 to obtain a 3D homology model of human Orai1 (Fig. 1A). We used loop modeling to add the two extracellular loops and one intracellular loop that are unresolved in the *Drosophila* crystal structure. To test the stability of the human Orai1 model in a lipid bilayer and examine its dynamics, we performed 100 ns molecular dynamics simulations (fig. S1A,B). Initially, the simulation included one Ca^{2+} ion placed in the selectivity filter, near Glu^{106}, to stabilize the geometry of the selectivity filter during equilibration. Throughout the duration of the simulation, the hexameric channel maintained its secondary and tertiary structure and also maintained the structural symmetry of all six subunits (fig. S1A). When the simulations included 10 mM extracellular Ca^{2+}, we observed transient Ca^{2+} binding, involving Asp^{110} and Asp^{112} in extracellular loop1, which are adjacent to the selectivity filter [Fig. 1B,C (yellow balls); fig. S1C; movie S1]. In addition, the simulations indicated that the pore entrance exhibited Na^+ ion binding, however, this was rare, occurring with an occupancy of less than 2% [Fig. 1C (orange ball)].

Ion density calculations revealed two major ion-density peaks: One was approximately at position 9 nm and corresponded to the extracellular loop1 segment, and the second one was present in the membrane, approximately at position 7.5 nm, which matched the position of the selectivity filter (Fig. 1D). Hence, when simulated with a 10 mM extracellular Ca^{2+} concentration, binding of Ca^{2+} close to the pore entrance increases the local Ca^{2+} up to 2.5 M within a 2 nm^3 volume (fig. 1C, fig. S1C; see Materials and Methods for calculations). We called this the "Ca^{2+} accumulating region" (CAR). Based on the structure, the simulations predicted that the CAR is ~ 1.2 nm from the selectivity filter (Fig. 1D), which is composed of the ring of the six Glu^{106} in each subunit, and is separated from the selectivity filter by a local energy barrier (19) that shows as the dip between the two peaks at 7.5 nm (selectivity filter) and 9 nm (CAR) in Figure 1D.

We evaluated the importance of the Asp^{110} residue in coordinating extracellular Ca^{2+} by substituting this aspartate with alanine. Simulations of the Orai1-D110A mutant revealed a shift of the Ca^{2+} ion contacts from Asp^{110} to Asp^{112} and Asp^{114} (Fig. 1E). Hence, we observed an ~0.6-nm increase in the distance between the Ca^{2+} ions bound in CAR and in the selectivity filter, from a distance of 1.2 nm to 1.8 nm (Fig. 1D). Additionally, the presence of Na^+ ions became an even left frequent event in the D110A mutant, occurring in less than 1% of the simulations.

Mutating Asp^{110} in CAR of Orai1 impairs store depletion-induced Ca^{2+} influx at low concentrations of extracellular Ca^{2+}

To investigate the impact of CAR on Ca^{2+} permeation through Orai1, we compared Ca^{2+} currents in cells coexpressing STIM1 tagged with mCherry and either wild-type Orai1 or Orai1-D110A, both of which were tagged with enhanced yellow fluorescent protein (eYFP), in the presence of increasing extracellular Ca^{2+} concentrations. We performed whole-cell patch-clamp experiments in the coexpressing HEK 293 cells, and we evoked SOCE currents by passive store-depletion (20 mM EGTA in the pipette). Starting with 0.3 mM Ca^{2+} extracellular solution, we stepwise increased the extracellular Ca^{2+} concentration to 1 mM and then 10 mM. Whereas SOCE currents were low for cells expressing either Orai1-WT or Orai1-D110A in 0.3 mM extracellular Ca^{2+}, 1 mM Ca^{2+} doubled the SOCE current and 10

mM Ca^{2+} produced a five-fold increase in cells expressing Orai1 compared with the currents recorded in 0.3 mM Ca^{2+} (Fig. 2A). Comparatively, in cells coexpressing STIM1 and Orai1-D110A, 1 mM Ca^{2+} did not increase SOCE current from that detected in 0.3 mM Ca^{2+}, but 10 mM Ca^{2+} resulted in maximum SOCE currents that were similar to those observed in the cells expressing Orai1 (Fig. 2A).

Analysis of the current-voltage profiles showed that the wild-type channel exhibited the typical inward rectifying current-voltage profile and similar high reversal potentials at 1 mM and 10 mM Ca^{2+} solutions (Fig. 2A). On the contrary, the profile for wild-type Orai1 and Orai1-D110A channels obtained with 0.3 mM Ca^{2+} solution were atypical for SOCE, exhibiting a flat current-voltage profile at negative potentials (Fig. 2A). Thus, even though we performed current-voltage analysis from currents obtained from cells expressing either wild-type Orai1 or Orai1-D110A (Fig. 2A), we repeated the current analysis in a Na^+-free environment (substituted by impermeable TEA^+) to evaluate only Ca^{2+} permeation at low extracellular Ca^{2+} concentrations, because in the absence of Ca^{2+} and other divalent ions, Orai channels become permeable to monovalent cations (20, 21).

In the Na^+-free solutions, upon STIM1 activation by store depletion, Orai1 exhibited Ca^{2+} influx in the presence of 0.3 mM extracellular Ca^{2+} solution and exhibited stepwise increases in current with increasing concentrations of extracellular Ca^{2+} (Fig. 2B). In contrast, Orai1-D110A currents were undetectable at the lowest Ca^{2+} concentration and, compared to those obtained with wild-type Orai1 channels, were reduced in the presence of 1 mM and 2 mM extracellular Ca^{2+} and were similar in the presence of 10 mM extracellular Ca^{2+} (Fig. 2B). Current-voltage analysis showed that both channels exhibited inward-rectifying profiles with similar high reversal potentials (V_{rev}: > 70mV), but the Orai1-D110A channels were less responsive at low extracellular concentrations of Ca^{2+} (Fig. 2B). Hence, the absence of the negative charge of Asp^{110} in CAR reduced Ca^{2+} permeation through the Orai1 channel; only nonphysiological, artificially high 10 mM Ca^{2+} concentrations bypassed the loss of CAR.

We performed similar analysis with cells expressing STIM1 and either with the Orai1-D112A or Orai1-D114A mutants. The Orai1-D112A mutant produced slightly smaller currents at 1 mM and 10mM extracellular Ca^{2+} than wild-type Orai1 (Fig. 2C). The Orai1-D114A mutant produced currents with a high amount of variability, but the Orai1-D114A currents were slightly, but not significantly, greater than the currents produced by the wild-type Orai1 channel at 1 and 10 mM extracellular Ca^{2+} (Fig. 2C).

Mutating Glu^{84} in the putative CAR of Orai2 impairs SOCE currents

Comparison of the primary amino acid sequences of human Orai isoforms showed that not all of the negative residues of CAR are conserved between these isoforms; Orai2 only contains one charged residue (Orai2-Glu^{84}, analogous to Orai1-Asp^{110}) in its extracellular loop 1, and Orai3 contains glutamates and aspartates in CAR. We coexpressed mCherry-tagged STIM1 and eYFP-tagged Orai2 in HEK cells and observed SOCE currents that increased with stepwise increases in extracellular Ca^{2+} (Fig. 3A) and that were similar to those recorded from cells coexpressing mCherry-STIM1 and YFP-Orai1 (Fig. 2A). Instead of creating an E84A mutant in Orai2, we mutated Glu^{84} to glutamine in Orai2, to retain

similar side-chains yet lacking its negative charge. SOCE currents in cells coexpressing Orai2-E84Q and STIM1 were significantly reduced in the presence of 1 and 10 mM extracellular Ca^{2+} in comparison to currents obtained with cells coexpressing wild-type Orai2 and STIM1. Although nonphysiological, we examined currents produced when all extracellular cations were substituted by Ca^{2+} (110 mM) to achieve a maximum extracellular Ca^{2+} levels. Orai2-E84Q still yielded significantly reduced currents (Fig. 3A). Current-voltage traces from the cells expressing Orai2 (Fig. 3B) or Orai2-E84Q (Fig. 3C) with STIM1 showed that the channels exhibited high Ca^{2+} selectivity (V_{rev} >70mV), hence residue Glu^{84} in CAR of Orai2 enhanced Ca^{2+} permeation without affecting the selectivity filter. To confirm that the differences we observed in the SOCE currents were not the result of differences in the abundance of the expressed proteins, we determined the mean fluorescence intensities of each Orai construct. The eYFP-tagged wild-type Orai1 constructs, eYFP-tagged wild-type Orai2 constructs, and the eYFP-tagged mutants, as well as coexpressed mCherry-tagged STIM1, produced similar fluorescence intensities, indicating similar amounts of the proteins (fig. S1D, S1E) as well as similar plasma-membrane localization (fig. S1F).

Orai1 CAR maintains Ca^{2+}-dependent gene regulation in various cell systems

To investigate the functional importance of CAR for SOCE-mediated responses, we assessed the role of CAR in Orai1 in Ca^{2+}-dependent gene transcription. The transcription factor NFAT requires sustained cytosolic Ca^{2+} concentrations to trigger expression of several immune-response genes, including those encoding cytokines and chemokines (22). Hence, we monitored SOCE in HEK 293 cells expressing mCherry-tagged STIM1 together with either eYFP-tagged Orai1 or eYFP-tagged Orai1-D110A by imaging changes in the Ca^{2+}-sensitive dye Fura-2. We initiated depletion of Ca^{2+} from the endoplasmic reticulum with the SERCA (sarcoplasmic and endoplasmic reticulum Ca^{2+} ATPase) inhibitor thapsigargin, which resulted in a similar transient increase in cytosolic Ca^{2+} in the cells expressing STIM1 with either Orai1 or Orai1-D110A (Fig. 4A). Addition of extracellular 0.3 mM Ca^{2+} (Fig. 4A), 0.5 Ca^{2+} mM (fig. S2A), or 1 mM Ca^{2+} (fig. S2B) resulted in a sustained increase in cytosolic Ca^{2+} that was significantly higher in cells expressing Orai1 than in those expressing Orai1-D110A (fig. S2C). Mock-transfected cells lacked a SOCE peak at 0.3 mM Ca^{2+} (Fig. 4A).

We assessed the activation of green fluorescent protein (GFP)-tagged NFAT by its relocation from the cytosol into the nucleus (23) in HEK 293 cells coexpressing mCherry-STIM1 and eYFP-Orai1. Within the first 5 minutes after addition of thapsigargin, during store-depletion, NFAT remained in the cytosol. Subsequent addition of 0.3 mM Ca^{2+} stimulated the relocation of NFAT into the nucleus (Fig. 4B,C). Cells coexpressing STIM1 and Orai1-D110A exhibited reduced NFAT translocation in response to store depletion followed by the addition of 0.3 mM Ca^{2}, and NFAT translocation did not occur in mock-transfected cells exposed to thapsigargin followed by the addition of 0.3 mM Ca^{2+} (Fig. 4B,C).

To monitor the activity of endogenous NFAT, we expressed an NFAT-responsive RFP construct (NFAT reporter) in which the fluorophore is controlled by a CMV promoter and tandem repeats of the NFAT consensus binding site (24) together with, mCherry-STIM1, and

eYFP-Orai1 or eYFP-Orai1-D110A in RBL (rat basophilic leukemia) mast cells. These cells were subjected to 100 nM thapsigargin in either 0.3 mM or 1.8 mM extracellular Ca^{2+} for 3.5 hours, and then monitored the number of RFP positive cells, as well as the abundance of RFP as indicated by the intensity of the signal. Approximately 60-70% of the STIM1- and Orai1-positive cells exhibited RFP signal in response to store depletion followed by addition of media containing 0.3 or 1.8 mM Ca^{2+} (Fig. 4D). Although the percent of RFP-positive cells was similar at both extracellular Ca^{2+} concentrations (Fig. 4D), RFP intensity increased in 1.8 mM extracellular Ca^{2+} (Fig. 4D). In contrast, only 20% of the cells cotransfected with STIM1 and Orai1-D110A exhibited RFP fluorescence and this was unchanged by store-depletion followed by addition of 0.3 or 1.8 mM Ca^{2+} (Fig. 4D). Coexpression of STIM1 and Orai1 in store-depleted HEK 293 cells exposed to 0.3 mM extracellular Ca^{2+} or coexpression of STIM1 and Orai1-D110A in store-depleted HEK 293 cells exposed to 2 mM Ca^{2+} resulted in similar Ca^{2+} signals (Fig. 2B). Furthermore, both Orai1 and Orai1-D110A formed clusters with STIM1 (Fig. 4E), whereas only coexpression of Orai1 and STIM1 mediated NFAT-driven RFP expression.

To bypass the requirement for CAR in NFAT signaling that was stimulated by STIM1-Orai1-mediated or STIM1-Orai1-D110A-mediated SOCE, we repeated the experiment in medium containing 10 mM Ca^{2+}. Here, a similar percentage of RBL cells expressing STIM1 with Orai1 or Orai1-D110A exhibited NFAT-driven production of RFP (fig. S2D). As additional control experiments, we exposed the cells to 10 μM ionomycin to increase cytosolic Ca^{2+} concentration through direct Ca^{2+} transport through the ionophore (25). The percentage of cells with NFAT-stimulated RFP production was similar for cells expressing either STIM1 with Orai1 or with Orai1-D110A (fig. S2D).

As cells in the circulation, mast cells are exposed to relatively high external Ca^{2+} concentrations (1-2 mM). However, STIM/Orai channels have important roles in melanocytes and melanoma cells, which reside in the basal epidermal layer where the external Ca^{2+} is much lower (0.2-0.4 mM) (8, 9). Hence, to test the “universality” of Orai1 CAR, we evaluated NFAT-driven expression of RFP, using the NFAT reporter upon store depletion in melanoma cells also transfected to express mCherry-STIM1 and either eYFP-Orai1 or eYFP-Orai1-D110A and growing in 0.4 mM Ca^{2+}-containing medium. NFAT driven RFP expression in Orai1-D110A-overexpressing melanoma cells was significantly less than that in the Orai1-expressing cells (Fig. 4F). These experiments indicated that without the CAR in Orai1, SOCE-induced NFAT signaling is compromised in cells that are exposed to either relatively low or high physiological concentrations of Ca^{2+}.

Basic residues in extracellular loop3 interact with Orai1 CAR

The loop3 segment exhibited the highest fluctuations in the overall Orai1 structure (fig. S1B). Molecular dynamics simulations of Orai1 predicted that the aspartates in loop1 not only bound Ca^{2+} but also formed transient electrostatic interactions with four basic residues (Lys^{203}, Lys^{204}, Arg^{210}, and Lys^{214}) in the flexible loop3 that connects TM3 and TM4. Specifically, residue Arg^{210} in loop3 transiently coupled with Asp^{112}, the middle aspartate in loop1. The molecular dynamics simulations revealed intra- and intermonomer interactions (0.5 interactions per Orai1 channel on average; Fig. 5A), demonstrating that even in the

relatively short simulation time (~ last 50 ns of a 100 ns simulation), the system sampled conformations in which such contacts are possible.

To experimentally evaluate the electrostatic loop1 and loop3 interactions, we used a disulfide crosslinking approach. We substituted the residues that were observed as interacting in the simulations with cysteines and measured disulfide-bridge formation between two Orai1 subunits. An interaction would produce a dimeric band (50 kD) on Western blots, whereas cysteines that failed to crosslink would result in the appearance of monomers (25 kD). We individually mutated residues in loop1 (L109C to L119C) (Fig. 5B) and assessed intermolecular interactions between analogous positions within an Orai1 channel complex in a cysteine-free background. The highest proportion of crosslinking occurred when the cysteine substituted residues were closer to the pore-forming TM1 helix (D110C, A111C: 70-80% dimer); in comparison to cysteine substituted residues in the middle or distal segment (D112C, D114C, Y115C, and P117C: 30–50% dimer; and L119C <20% dimer) (Fig. 5C). Crosslinking of cysteines was reversible by addition of the reducing agent bis(2-mercaptoethyl)sulphone (BMS) (fig. S3A). In molecular dynamics simulations, we selected a specific loop1 residue in all 6 subunits of the Orai1 channel and measured their distances over 100 ns, to predict the potential to crosslink. Consistent with these biochemical experiments, molecular dynamics simulations revealed close time-dependent distances between loop1 residues next to TM1 (fig. S3B).

Similarly, we individually mutated the 15 consecutive residues along loop3 of Orai1 to cysteines (Fig. 5D), and analysed their propensity to dimerize in crosslinking experiments (fig. S4A). These mutants exhibited a bell-shaped dimerization profile (Fig. 5E), indicating that residues in the middle of loop3 (Lys^{214} to Ser^{225}) preferentially interacted with other loop3 subunits, compared with the amino acids closer to the TM3 or TM4 helices. Consistently, the residues in the middle of loop3 showed largest flexibility in molecular dynamics simulations (fig. S4B)

Next, we tested for the simulated loop1/loop3 interaction between Asp^{112} in loop1 and Arg^{210} in loop3 by creating a cysteine double mutant (Orai1-D112C-R210C) and assessing its ability to form disulfide-bridged oligomers. We observed two bands in Western blots: one predominant band at 125 kD, corresponding to a pentamer, and a second at 25 kD, corresponding to a monomer (Fig. 6A, fig. S4C). These data indicated efficient coupling of the Asp^{112} and Arg^{210} positions between different Orai subunits. We also examined if the architecture of the Orai1 channel favored the interaction between D112C and R210C rather than the interaction between R210C in loop3 with residues adjacent to D112C in loop1 (Orai1-A111C-R210C and Orai1-H113C-R210C, fig. S4D) or the interaction between D112C in loop1 with the residue adjacent to R210C in loop3 (Orai1-D112C-A221C, Fig. 6A). Only the Orai1-D112C-R210C double mutant produced hexamers, the other double cysteine mutants yielded mainly monomers and dimers ((Fig. 6A, fig. S4A). Hence, these crosslinking experiments revealed a preferential geometry for heteromeric interaction between Asp^{112} and Arg^{210}.

Loop3 interaction competes with Ca^{2+} binding in the Orai1 CAR

This potential loop3-loop1 coupling within human Orai1 might affect CAR by competing with Ca^{2+} binding and thus Ca^{2+} permeation. Even cells that were not exposed to the crosslinking reagent CuP exhibited efficient crosslinking of the Orai1-D112C-R210C double mutant (fig. S4D), which would force loop3 into a conformation that moves loop3 close to the pore entrance. We monitored SOCE, induced by passive store depletion with 20 mM EGTA in 10 mM Ca^{2+}-containing medium, in HEK 293 cells expressing mCherry-STIM1 with eYFP-Orai1-D112C-R210C, eYFP-Orai1-D112C, or eYFP-Orai1-R210C. Store-dependent currents of crosslinked Orai1-D112C-R210C were significantly reduced in comparison to those mediated by STIM1 and Orai1 (Fig. 6B). Breaking the disulfide bonds with BMS resulted in a 300% increase in the Orai1-D112C-R210C-mediated currents (Fig. 6B,C), which were similar to maximum currents obtained with cells expressing Orai1-D112C and STIM1 and exceeding those obtained with cells expressing Orai1 and STIM1 (Fig. 6B). In analogous experiments, none of the loop3 cysteine mutants (each of which produced ≤ 40% increase in average current after BMS treatment) (Fig. 6D, fig. S5A) or the single loop1 (each of which produced ≤ 20% increase in current after BMS treatment) (Fig. 6E) nor adjacent double cysteine mutants (Orai1-A111C-R210C and Orai1-H113C-R210C, which produced ≤ 10% increase in current after BMS treatment) (fig. S5B) exhibited such a marked BMS-dependent current increase. Hence, the forced D112C to R210C interaction had the greatest effect on Ca^{2+} permeation.

To investigate the competitive Ca^{2+} and loop3 interaction with Orai1 CAR, we tested the BMS-dependent increase in Orai1-D112C-R210C currents in different concentrations of extracellular Ca^{2+}. In a 1 mM Ca^{2+}-containing solution, BMS increased Orai1-D112C-R210C currents by 400% (Fig. 6F,G) and in a 10 mM Ca^{2+}-containing solution BMS increased Orai1-D112C-R210C currents by 300% (Fig. 6G); whereas currents only increased by 100% when the cells were exposed to BMS in the presence of sodium-based extracellular solution (Fig. 6G). The 100% increase by BMS in a sodium-based solution indicated that loop3 binding to residues in the CAR of loop1 has a steric effect on Orai1 Ca^{2+} permeation, and the additional 300% in a 1 mM Ca^{2+}-containing solution indicated that loop3 binding to CAR has a Ca^{2+}-dependent effect on Orai1 permeation. We speculate that an enhanced Asp^{112} – Arg^{210} interaction might affect the orientation or flexibility of the Asp^{110} sidechain and hence the binding of Ca^{2+} ions to CAR.

Statistical analysis of interactions in molecular dynamics simulations of human Orai1 predicted that Asp^{110} rarely made interactions with other residues, thus would rarely participate in the loop3 interaction (fig. S6A) and frequently interacted with Ca^{2+} or Na^{+} (fig. S6B). The simulations predicted that Asp^{112} did not have a clear preference, making contacts to the basic residues in loop3 as well as to cations (fig. S6A, B). On the contrary, the simulations predicted that Asp^{114} nearly exclusively contacted positively charged residues of loop3 (fig. S6A) and made almost no contacts with Ca^{2+} or Na^{+} (fig. S6B). Specifically, Asp^{114} interactions were predicted to occur with Lys^{203}, Lys^{204}, and Lys^{214} (fig. S6C). In the simulations, the Asp^{114}-Lys^{214} interaction (0.5 interactions on average per Orai1 channel) was only observed within the same Orai1 subunit (fig. S6C). Consistent with the simulations, intramolecular crosslinking of D114C-K214C interfered with Orai1-K214C

dimerization (fig. S6D). This interloop interaction, however, did not affect Orai1-D114C-K214C-mediated SOCE currents monitored in the presence of 10 mM extracellular Ca^{2+} (fig. S6E). Thus, these data indicate that the loop3 interaction with Asp^{112} but not Asp^{114} regulates Ca^{2+} permeation of Orai1.

We attempted to form an Orai1 channel with an even more efficient CAR by mutating both Arg^{210} and Lys^{214} to alanines to restrict the competitive loop3 binding with Ca^{2+} in the CAR. Indeed, compared with the simulations of wild-type Orai1 (Fig. 1C), simulations of an Orai1-R210A-K214A mutant channel exhibited additional bound Ca^{2+} ions to Asp^{112} and Asp^{114} (Fig. 7A), and a broadened CAR peak in the horizontal line scan (Fig. 7B). This additional CAR peak was not observed for single Orai1-R210A and Orai1-K214A mutations (Fig. 7B). However, for Orai1-R210A, Ca^{2+} was more frequently present between the selectivity filter and CAR (Fig. 7B) where it might facilitate Ca^{2+} movement into the channel. When expressed as fusion proteins (mCherry for STIM1 and eYFP for the Orai1 constructs) in HEK 293 cells, store-operated currents were significantly increased for STIM1 and Orai1-R210A-K214A or STIM1 and Orai1-R210A in comparison to the currents detected for STIM1 and wild-type Orai1 in 0.3 mM extracellular Ca^{2+} (Fig. 7C). In both Orai1 loop3 mutants, a stepwise increase to 1 mM Ca^{2+} enhanced permeation (significantly for Orai1-R210A-K214A), whereas at 10 mM extracellular Ca^{2+}, the wild-type Orai1 channels and the channels with the Orai1 loop3 mutants reached a similar maximum value (Fig. 7C). These experiments revealed that basic loop3 residues can compete with Ca^{2+} for similar binding sites at the extracellular CAR and thereby limit Ca^{2+} permeation.

Discussion

Our results identified a previously unknown region, CAR, that enhances Ca^{2+} permeation by promoting the accumulation of Ca^{2+} at the pore entrance of the human Orai1 channel. CAR is formed by aspartates that dynamically bind Ca^{2+} ions. This extracellular Ca^{2+}-binding domain was predicted to increase the local Ca^{2+} concentration at the outer channel mouth, for example from 10 mM to 2.5 M, and thereby enhance the driving force for Ca^{2+} permeation. CAR is positioned only ~1.2 nm from the selectivity filter. Mutation of CAR residue Asp^{110} increased the distance between these two Ca^{2+}-binding structures to ~ 1.8 nm and suppressed Ca^{2+} permeation at physiological extracellular Ca^{2+} concentrations. Hence, our data indicated that the Ca^{2+}-permeation pathway of Orai channels requires the enhanced local Ca^{2+} concentration generated by CAR to induce Ca^{2+} passage through the narrowest part of the pore. Such a Ca^{2+}-binding structure has not been identified in other highly Ca^{2+}-selective plasma membrane channels, including voltage-gated Ca^{2+} channels and transient receptor potential channels (26–28). In comparison to voltage-gated L-type channels, which exhibit a single-channel conductance of 2.6 pS (29), Orai1 and CRAC channels containing Orai1 have a much lower single-channel conductance that is 8-9 fS (14, 30). Hence, for Orai1 channels, the cytosolic Ca^{2+} concentrations only achieve micromolar Ca^{2+} concentrations within a few nm from the pore, thereby creating local Ca^{2+} microdomains (31). Orai mutants lacking CAR would diminish these functional Ca^{2+} microdomains that are critical for effective and selective downstream signaling. Thus, Orai1 CAR represents a channel-intrinsic mechanism to drive local Ca^{2+} signaling.

Two high resolution structures of the ryanodine receptor suggested that luminal loops close to the selectivity filter could attract Ca^{2+} for permeation and may partially account for Ca^{2+} release in response to store overload (32, 33). Similar to CAR in Orai1, these luminal loops in the ryanodine receptor may enhance Ca^{2+} influx.

The aspartate residues that form CAR have been reported to contribute to Ca^{2+} selectivity, because double or triple aspartate mutations in Orai1 lead to channels that conduct nonselective cation currents (16, 34). However, single Orai1 aspartate mutations yield Ca^{2+}-selective currents [(17, 35) and the current work]. In the present study, an engineered Orai2 that lacked all negative sidechains within CAR still retained Ca^{2+} selectivity yet, exhibited substantially reduced Ca^{2+} currents. Hence, this Orai2 mutant functioned in a mode in which Ca^{2+} selectivity was uncoupled from CAR.

CAR interactions with the outer loop3, mediated by Asp^{112} (loop1) and Arg^{210} (loop3) residues suppressed Ca^{2+} permeation, in a Ca^{2+}-dependent, as well as a steric, manner. Consistent with this effect of the interaction of loop3 with CAR, mutations that prevented the loop1 and loop3 interaction or the presence of a reducing agent for channels that breaks engineered crosslinked residues resulted in channels that exhibited enhanced Ca^{2+} permeation. Neither the basic loop3 residues nor the number of CAR residues are conserved among the human Orai family, suggesting that the differences in the sequence of the pore entrance may fine-tune Orai isoform-specific Ca^{2+} permeation.

The enhanced Ca^{2+} concentrations generated by CAR have important physiological consequences, particularly at a low environmental Ca^{2+}. To translocate to the nucleus and initiate gene transcription, the Ca^{2+}-dependent transcription factor NFAT requires sustained Ca^{2+} signals (36). At an extracellular 2 mM Ca^{2+}, currents of an Orai1-D110A CAR mutant were 2-fold reduced and exhibited similar currents as those of wild-type Orai1 at 0.3 mM Ca^{2+}. Despite these similar global Ca^{2+} signals, only wild-type Orai1 triggered NFAT-mediated gene expression in mast cells. Local Ca^{2+} microdomains stimulate consistent NFAT signaling, because even a similar global increase in Ca^{2+} concentration can result in divergent NFAT signaling (23, 37). One predominant factor is the formation of Orai1 clusters (37). Our results revealed that CAR determines the Ca^{2+} driving force and thus Ca^{2+} microdomain signaling as indicated by the impaired NFAT response of cells expressing STIM1 and Orai1-D110A. Consequently, cooperativity of diminished Ca^{2+} microdomains of Orai1-D110A Ca^{2+} channels might affect NFAT signaling in a manner similar to that observed with conditions that abolished cluster formation by Orai1 channels (37). In addition, we found that melanoma cells required CAR to enable NFAT signaling at physiologically low 0.4 mM Ca^{2+} concentrations. Hence, our data showed that the Orai1 CAR contributes to the formation of functional Ca^{2+} microdomains that are strictly required for NFAT signaling (38).

The data presented here show that the Orai channel architecture with a close distance between CAR and the Ca^{2+} selectivity filter enables Ca^{2+} signaling even when environmental Ca^{2+} is low, as in the basal epidermal layer, thereby explaining an ubiquitous cellular Ca^{2+} entry route.

Materials and Methods

3D model of human Orai1

The published *D. melanogaster* Orai1 crystal structure (PDB ID: 4HKR) was used to construct a full atomistic model of human Orai1. Two extracellular loops and one intracellular loop are unresolved in the *Drosophila* crystal structure and were modeled by retrieving loop conformations bridging two sets of anchor residues from the Protein Data Bank.The sequence identity is 63% between human and *D. melanogaster* (78% sequence similarity) within the aligned region, therefore, homology modeling can produce a reasonable 3D model with an estimated resolution of ~ 2 Å. Homology modelling was performed in Yasara (39), using the standard macro hm_built.mcr with the FixModelRes option to constrain conserved residues. The final model has an overall quality Z-score of -1.931 as given by Yasara, 96.1% of the residues in the most favoured regions of the Ramachandran plot and a G-factor of 0.17 as calculated by Procheck (40).

Molecular dynamics simulations

The human Orai1 model was inserted into a pre-equilibrated palmitoyloleoylphosphatidylcholine (POPC) bilayer consisting of 512 lipid molecules using the inflategro method (41). Copies of the model were modified by introducing point mutations in all six monomers using Yasara. The protonation state of histidine residues was predicted in WHATIF (42). Simulations were performed with the GROMACS 4.6.1/4.6.3 software (43, 44). POPC molecules were described by Berger parameters for lipids (45) converted into the format of the OPLS (Optimized Potentials for Liquid Simulations) all-atom force field (46), following the procedure proposed by Neale (http://www.pomeslab.com/files/lipidCombinationRules.pdf. The protein-lipid system was solvated with water molecules described by the simple point charge model of water (46) and counter-ions were added to achieve electric neutrality. Additionally, calcium-, sodium- and chloride-ions were added to a final concentration of 10mM $CaCl_2$ and 8mM NaCl. Molecular dynamics simulations were carried out in the isothermal–isobaric (NPT) ensemble employing a 2 fs time step. Periodic boundary conditions were used. Initial velocities were assigned by applying a Maxwell distribution at 310 K. Lennard-Jones and electrostatic interactions were cut off at a distance of 10.0 Å and the long-range electrostatic interactions were computed employing the particle-mesh Ewald method (47). The temperature was kept at 310 K using the velocity rescale thermostat and the pressure was kept constant at 1 bar by weak coupling (T = 2.0 ps) to a pressure bath using the Parrinello–Rahman algorithm (48), which was employed with a semi-isotropic mode. Bond lengths were constrained using the LINCS method (49). Simulations were carried out for 100 ns, and averaged traces include 4 independent simulations. All data analysis was done using GROMACS utilities. Ion density numbers were calculated from horizontal stacks across the simulation box through the channel, which means in Z direction, using g_density. To avoid artifacts from fluctuations of the box in Z-direction, every system was centered to a common reference point for the center of mass of the protein with a constant box size using an in-house script (provided with the Movie S1 file in the Supplementary Materials). Ions stuck in the membrane were removed from the calculation to reduce the noise level. Density maps were generated with

g_densmap and color scale was normalized according to the percentage of occupancy with blue color corresponding to a Ca^{2+} ion occupying the position in 100% of simulation time.

All data were processed and plots were prepared using Xmgrace [http://plasma-gate.weizmann.ac.il/Grace/]. For visualization of molecular dynamics trajectories and preparation of figures of protein overview VMD (50) was utilized. Calculation of local Calcium concentration in CAR, with N = 3 Ca^{2+} ions, N_A the Avogadro constant ($6{,}022*10^{23}$ mol^{-1}) and volume v_i (2 * 2 * 0,5 nm^3). Amount of substance $n_i = N/N_A = 0.5*10^{-23}$ mol, Molarity n_i/v_i = 2.5M.

Plasmids

Human Orai1 (Orai1; accession number NM_032790.3) was kindly provided by A. Rao (Harvard Medical School). N-terminally tagged Orai1 constructs were cloned into the SalI and SmaI restriction sites of pECFP-C1 and pEYFP-C1 expression vectors (Clontech). Human STIM1 (STIM1; accession number NM_003156) N-terminally ECFP- and EYFP-tagged was kindly provided by T. Meyer, Stanford University. GFP-NFAT was kindly provided by Ralph Kehlenbach (Scripps Research Institute). pNFAT-TA-mRFP (NFAT-driven RFP expression) was kindly provided by Y. Usachev (University of Iowa). hOrai1 Δ1-64, N223A, cysteine-free was cloned into the T/A site of pcDNA3.1V5-His/TOPO vector (Invitrogen) without any additional tag by PCR amplification. For crosslinking mutants, a cysteine-free Orai1 (C126V, C143V, C195V) analogous to that described in Zhou *et al.* (51), was generated, the glycosylation site was replaced by an alanine (N223A) and the nonconserved N-terminal region removed (Δ1-64) to gain a single protein of 25 kD on SDS-PAGE, representing a monomer. Point mutations (N223A, C126V, C143V, C195V and all engineered cysteine substitutions) were introduced using the QuikChange site-directed mutagenesis kit (Stratagene). The integrity of all resulting mutants was confirmed by sequence analysis (Eurofins Genomics). For electrophysiological measurements, cysteine/alanine substitutions were introduced into an eYFP-hOrai1 construct (peYFP-C1: Clontech) and an eYFP-hOrai2 construct. Neither the N-terminal region nor the glycosylation site is required for CRAC channel function (15, 52, 53). The modified Orai1 mutants, except of Orai1-P201C, when coexpressed with STIM1 yielded store-dependent activation of inward-rectifying Ca^{2+} currents (as representatively shown in Fig. 6B, C). For all tested mutants correct plasma membrane expression was monitored by fluorescence microscopy (fig. S1F).

Membrane preparation

HEK293 cells cultured in 12-mm dishes were transfected with 15 μg plasmid using Transfectin lipid reagent (Biorad) following the manufacturer's instructions. Twenty four hours after transfection, cells were harvested and washed twice in an HBSS (Hank's balanced salt solution) buffer containing 1 mM EDTA. After centrifugation (1000g/2min), cell pellets were resuspended in homogenization buffer [25mM Tris HCl pH7.4, 50mM NaCl, protease inhibitor (Roche)] and incubated on ice for 15 min. Lysed cells were passed 10 times through a 27G ½" needle and centrifuged at 1000g for 15 min at 4°C to pellet debris. 21 μl of the supernatant were analyzed by 12% SDS-PAGE either without or after the addition of 1 mM CuP (Cu-Phenanthroline) or 5 mM BMS.

Disulfide Crosslinking

To 21 μl of supernatant 1mM $CuSO_4$/1.3mM o-phenanthroline final concentration (Sigma) was added, incubated 10 min on ice, and reactions were stopped by the addition of an equal volume of quenching solution [50mM Tris HCl, 20mM N-ethylmaleimide, 20mM EDTA, pH7.4]. Samples were mixed with nonreducing Laemmli's buffer, heated 15 min at 55°C, and subjected to a 12% SDS PAGE. Separated proteins were transferred to a nitrocellulose membrane and immunoblotted with an antibody recognizing Orai1 (Sigma). Each experiment was performed at least 5 independent times. The quantification of percentage of crosslinking was calculated with the program ImageJ (National Institute of Mental Health).

Electrophysiological recordings

HEK293 cells were transfected (Transfectin, Bio-Rad) with 1 μg mCherry-STIM1 and 0.5 μg DNA of eYFP-Orai1 constructs. Electrophysiological experiments were performed 24 to 34 hours after transfection, using the patch-clamp technique in whole-cell recording configurations at 21–25°C. An Ag/AgCl electrode was used as reference electrode. Voltage ramps were applied every 5 s from a holding potential of 0 mV, covering a range of –90 to 90 mV over 1 s. For passive store depletion, the internal pipette solution included (in mM): 145 Cs methane sulphonate, 20 EGTA, 10 HEPES, 8 NaCl, 3.5 $MgCl_2$, pH 7.2. Standard extracellular solution consisted of (in mM) 145 NaCl, 10 HEPES, 10 $CaCl_2$, 10 glucose, 5 CsCl, 1 $MgCl_2$, pH 7.4. Where indicated, extracellular $CaCl_2$ was decreased to 0.3 mM or 1 mM, or monovalent ions were substituted by TEACl. A liquid junction potential correction of +12 mV was applied, resulting from a Cl^--based bath solution and a sulphonate-based pipette solution. All currents were leak corrected by subtracting the initial voltage ramps obtained shortly following break-in with no visible current activation from the measured currents. Averaged currents include n = 6 -23 experiments.

Fura-2 Calcium Microscopy

HEK293 cells were transfected (Transfectin, Bio-Rad) with 0.7 μg mCherry-STIM1 and eYFP-Orai1 or eYFP-Orai2 constructs or mutants. Twenty to 24 hours after transfection, the cells were loaded with 2 μM fura 2-AM (Sigma-Aldrich)for 20 min at 20 ºC in a standard Ca^{2+}-free extracellular solution: in [mM]: 140 NaCl, 5 KCl, 1 $MgCl_2$, 10 HEPES, 10 Glucose. The cells were washed three times and dyes were allowed to de-esterify for 15 minutes at 20°C. Individual cells were excited at 340 and 380 nm and emission was recorded at 505 nm with an inverted Axiovert 100 TV microscope (Zeiss, Germany). Changes in $[Ca^{2+}]_i$ were monitored using the fura-2 340/380 fluorescence ratio and calibrated according to the method established by Grynkiewicz *et al.* (54). Ca^{2+} entry is presented as nM·s and was estimated using the integral of the rise in $[Ca^{2+}]_i$ for 30 min after addition of $CaCl_2$ (300 μM, 500 μM, 1 mM, or 2 mM) corrected by subtraction of the integral over the same period for stimulation in the absence of external Ca^{2+} (with 100 μM EGTA). Averaged traces include n = 19 – 40 cells.

NFAT translocation

A QLC100 Real-Time Confocal System (VisiTech Int., UK) connected to two Photometrics CoolSNAPHQ monochrome cameras (Roper Scientific) and a dual port adapter (dichroic:

505lp; cyan emission filter: 485/30; yellow emission filter: 535/50; Chroma Technology Corp.) was used for recording fluorescence images. This system was attached to an Axiovert 200M microscope (Zeiss, Germany) in conjunction with two diode lasers (445 nm, 515 nm) (Visitron Systems). Image acquisition and control of the confocal system was performed with a Visiview 2.1.1 software (Visitron Systems). Extracellular solution identical as for fluorescence microscopy but with 0.3 mM or 1.8 mM $CaCl_2$. Averaged experiments include 5 – 12 experiments.

NFAT-driven RFP expression

RBL cells were electroporated with 6 μg STIM1, 6 μg YFP-Orai1 or YFP-Orai1-D110A, and 12 μg pNFAT-TA-mRFP. Twenty four hours after electroporation, RBL cells were treated with 100 nM TG for 3.5 hours in a 0.3 mM or 1.8 mM Ca^{2+}-containing medium. Cells expressing both YFP-Orai1 and NFAT-driven RFP were monitored with an Axiovert 100 TV microscopy, and fluorescence was recorded from individual cells with excitation of 514 and 565 nm, respectively.

Data and materials availability

The structural model for human Orai1 is available in the Model Archive (modelarchive.org) with the accession code ma-akdjp. The Perl script for centering the system to a common reference point for the density number calculations is available in the Supplementary Materials.

Supplementary Material

Refer to Web version on PubMed Central for supplementary material.

Acknowledgements

We wish to thank Thomas Stockner (Medical University of Vienna) and David Reha (Academy of Sciences of the Czech Republic) for technical assistance with lipid parametrization and data analysis, respectively. Human Orai1 was provided by A. Rao (Harvard Medical School).

Human STIM1 N-terminally ECFP- and EYFP-tagged was provided by T. Meyer (Stanford University). GFP-NFAT was provided by Ralph Kehlenbach (Scripps Research Institute). pNFAT-TA-mRFP was provided by Y. Usachev (University of Iowa).

Funding: This work was funded by projects from the Austrian Science Fund (FWF): V286-B21 to I.F., P26067 and P28701 to R.S., P25172 to C.R., P25210 and P27641 to I.D., M01506000 to I.J.P., P28498 to M.M, and BMWF HRSM project to C.R., from the Czech Science Foundation (13-21053S) to R.E, and the German Research Foundation (DFG): SFB1027 project C4 to I.B.

References

1. Feske S. ORAI1 and STIM1 deficiency in human and mice: roles of store-operated Ca2+ entry in the immune system and beyond. Immunol Rev. 2009; 231:189–209. [PubMed: 19754898]
2. Di Capite J, Parekh AB. CRAC channels and Ca2+ signaling in mast cells. Immunol Rev. 2009; 231:45–58. [PubMed: 19754889]
3. Feske S, Skolnik EY, Prakriya M. Ion channels and transporters in lymphocyte function and immunity. Nat Rev Immunol. 2012; 12:532–547. [PubMed: 22699833]

4. Hogan PG, Lewis RS, Rao A. Molecular basis of calcium signaling in lymphocytes: STIM and ORAI. Annu Rev Immunol. 2010; 28:491–533. [PubMed: 20307213]
5. Bergmeier W, Weidinger C, Zee I, Feske S. Emerging roles of store-operated Ca(2)(+) entry through STIM and ORAI proteins in immunity, hemostasis and cancer. Channels (Austin). 2013; 7:379–391. [PubMed: 23511024]
6. Prevarskaya N, Skryma R, Shuba Y. Calcium in tumour metastasis: new roles for known actors. Nat Rev Cancer. 2011; 11:609–618. [PubMed: 21779011]
7. Ruhle B, Trebak M. Emerging roles for native Orai Ca2+ channels in cardiovascular disease. Curr Top Membr. 2013; 71:209–235. [PubMed: 23890117]
8. Stanisz H, Stark A, Kilch T, Schwarz EC, Muller CS, Peinelt C, Hoth M, Niemeyer BA, Vogt T, Bogeski I. ORAI1 Ca(2+) channels control endothelin-1-induced mitogenesis and melanogenesis in primary human melanocytes. J Invest Dermatol. 2012; 132:1443–1451. [PubMed: 22318387]
9. Stanisz H, Saul S, Muller CSL, Kappl R, Niemeyer BA, Vogt T, Hoth M, Roesch A, Bogeski I. Inverse regulation of melanoma growth and migration by Orai1/STIM2-dependent calcium entry. Pigm Cell Melanoma R. 2014; 27:442–453.
10. Dolmetsch RE, Lewis RS, Goodnow CC, Healy JI. Differential activation of transcription factors induced by Ca2+ response amplitude and duration. Nature. 1997; 386:855–858. [PubMed: 9126747]
11. Dolmetsch RE, Xu K, Lewis RS. Calcium oscillations increase the efficiency and specificity of gene expression. Nature. 1998; 392:933–936. [PubMed: 9582075]
12. Hou X, Pedi L, Diver MM, Long SB. Crystal structure of the calcium release-activated calcium channel Orai. Science. 2012; 338:1308–1313. [PubMed: 23180775]
13. McNally BA, Somasundaram A, Yamashita M, Prakriya M. Gated regulation of CRAC channel ion selectivity by STIM1. Nature. 2012; 482:241–245. [PubMed: 22278058]
14. Zhang SL, Yeromin AV, Hu J, Amcheslavsky A, Zheng H, Cahalan MD. Mutations in Orai1 transmembrane segment 1 cause STIM1-independent activation of Orai1 channels at glycine 98 and channel closure at arginine 91. Proc Natl Acad Sci U S A. 2011; 108:17838–17843. [PubMed: 21987804]
15. Prakriya M, Feske S, Gwack Y, Srikanth S, Rao A, Hogan PG. Orai1 is an essential pore subunit of the CRAC channel. Nature. 2006; 443:230–233. [PubMed: 16921383]
16. Vig M, Beck A, Billingsley JM, Lis A, Parvez S, Peinelt C, Koomoa DL, Soboloff J, Gill DL, Fleig A, Kinet JP, et al. CRACM1 multimers form the ion-selective pore of the CRAC channel. Curr Biol. 2006; 16:2073–2079. [PubMed: 16978865]
17. Yeromin AV, Zhang SL, Jiang W, Yu Y, Safrina O, Cahalan MD. Molecular identification of the CRAC channel by altered ion selectivity in a mutant of Orai. Nature. 2006; 443:226–229. [PubMed: 16921385]
18. Derler I, Fahrner M, Carugo O, Muik M, Bergsmann J, Schindl R, Frischauf I, Eshaghi S, Romanin C. Increased Hydrophobicity at the N Terminus/Membrane Interface Impairs Gating of the Severe Combined Immunodeficiency-related ORAI1 Mutant. Journal of Biological Chemistry. 2009; 284:15903–15915. [PubMed: 19366689]
19. Dong H, Fiorin G, Carnevale V, Treptow W, Klein ML. Pore waters regulate ion permeation in a calcium release-activated calcium channel. Proc Natl Acad Sci U S A. 2013; 110:17332–17337. [PubMed: 24101457]
20. Peinelt C, Vig M, Koomoa DL, Beck A, Nadler MJ, Koblan-Huberson M, Lis A, Fleig A, Penner R, Kinet JP. Amplification of CRAC current by STIM1 and CRACM1 (Orai1). Nat Cell Biol. 2006; 8:771–773. [PubMed: 16733527]
21. Lepple-Wienhues A, Cahalan MD. Conductance and permeation of monovalent cations through depletion-activated Ca2+ channels (ICRAC) in Jurkat T cells. Biophys J. 1996; 71:787–794. [PubMed: 8842217]
22. Srikanth S, Gwack Y. Orai1-NFAT signalling pathway triggered by T cell receptor stimulation. Mol Cells. 2013; 35:182–194. [PubMed: 23483280]
23. Kar P, Nelson C, Parekh AB. Selective activation of the transcription factor NFAT1 by calcium microdomains near Ca2+ release-activated Ca2+ (CRAC) channels. J Biol Chem. 2011; 286:14795–14803. [PubMed: 21325277]

24. Kim MS, Usachev YM. Mitochondrial Ca2+ cycling facilitates activation of the transcription factor NFAT in sensory neurons. J Neurosci. 2009; 29:12101–12114. [PubMed: 19793968]
25. Kar P, Parekh AB. Distinct spatial Ca2+ signatures selectively activate different NFAT transcription factor isoforms. Mol Cell. 2015; 58:232–243. [PubMed: 25818645]
26. Voets T, Janssens A, Droogmans G, Nilius B. Outer pore architecture of a Ca2+-selective TRP channel. J Biol Chem. 2004; 279:15223–15230. [PubMed: 14736889]
27. Liao M, Cao E, Julius D, Cheng Y. Structure of the TRPV1 ion channel determined by electron cryo-microscopy. Nature. 2013; 504:107–112. [PubMed: 24305160]
28. Tang L, Gamal El-Din TM, Payandeh J, Martinez GQ, Heard TM, Scheuer T, Zheng N, Catterall WA. Structural basis for Ca2+ selectivity of a voltage-gated calcium channel. Nature. 2014; 505:56–61. [PubMed: 24270805]
29. Church PJ, Stanley EF. Single L-type calcium channel conductance with physiological levels of calcium in chick ciliary ganglion neurons. J Physiol. 1996; 496(Pt 1):59–68. [PubMed: 8910196]
30. Zweifach A, Lewis RS. Rapid inactivation of depletion-activated calcium current (ICRAC) due to local calcium feedback. J Gen Physiol. 1995; 105:209–226. [PubMed: 7760017]
31. Parekh AB. Ca(2+) microdomains near plasma membrane Ca(2+) channels: impact on cell function. J Physiol-London. 2008; 586:3043–3054. [PubMed: 18467365]
32. Zalk R, Clarke OB, des Georges A, Grassucci RA, Reiken S, Mancia F, Hendrickson WA, Frank J, Marks AR. Structure of a mammalian ryanodine receptor. Nature. 2015; 517:44–49. [PubMed: 25470061]
33. Yan Z, Bai XC, Yan C, Wu J, Li Z, Xie T, Peng W, Yin CC, Li X, Scheres SH, Shi Y, et al. Structure of the rabbit ryanodine receptor RyR1 at near-atomic resolution. Nature. 2015; 517:50–55. [PubMed: 25517095]
34. Beck A, Fleig A, Penner R, Peinelt C. Regulation of endogenous and heterologous Ca(2)(+) release-activated Ca(2)(+) currents by pH. Cell Calcium. 2014; 56:235–243. [PubMed: 25168908]
35. McNally BA, Yamashita M, Engh A, Prakriya M. Structural determinants of ion permeation in CRAC channels. Proc Natl Acad Sci U S A. 2009; 106:22516–22521. [PubMed: 20018736]
36. Kar P, Nelson C, Parekh AB. CRAC channels drive digital activation and provide analog control and synergy to Ca(2+)-dependent gene regulation. Curr Biol. 2012; 22:242–247. [PubMed: 22245003]
37. Samanta K, Kar P, Mirams GR, Parekh AB. Ca(2+) Channel Re-localization to Plasma-Membrane Microdomains Strengthens Activation of Ca(2+)-Dependent Nuclear Gene Expression. Cell Rep. 2015; 12:203–216. [PubMed: 26146085]
38. Kar P, Samanta K, Kramer H, Morris O, Bakowski D, Parekh AB. Dynamic assembly of a membrane signaling complex enables selective activation of NFAT by Orai1. Curr Biol. 2014; 24:1361–1368. [PubMed: 24909327]
39. Krieger E, Koraimann G, Vriend G. Increasing the precision of comparative models with YASARA NOVA--a self-parameterizing force field. Proteins. 2002; 47:393–402. [PubMed: 11948792]
40. Laskowski RA, Macarthur MW, Moss DS, Thornton JM. Procheck - a Program to Check the Stereochemical Quality of Protein Structures. J Appl Crystallogr. 1993; 26:283–291.
41. Kandt C, Ash WL, Tieleman DP. Setting up and running molecular dynamics simulations of membrane proteins. Methods. 2007; 41:475–488. [PubMed: 17367719]
42. Vriend G. What If - a Molecular Modeling and Drug Design Program. J Mol Graphics. 1990; 8:52–&.
43. Van der Spoel D, Lindahl E, Hess B, Groenhof G, Mark AE, Berendsen HJC. GROMACS: Fast, flexible, and free. Journal of Computational Chemistry. 2005; 26:1701–1718. [PubMed: 16211538]
44. Hess B. GROMACS 4: Algorithms for highly efficient, load-balanced, and scalable molecular simulation. Abstr Pap Am Chem S. 2009; 237
45. Berger O, Edholm O, Jahnig F. Molecular dynamics simulations of a fluid bilayer of dipalmitoylphosphatidylcholine at full hydration, constant pressure, and constant temperature. Biophysical Journal. 1997; 72:2002–2013. [PubMed: 9129804]
46. Berendsen HJCP, M JP, van Gunsteren WF, Hermans J. Intermolecular Force. 1981

47. Darden T, York D, Pedersen L. Particle Mesh Ewald - an N.Log(N) Method for Ewald Sums in Large Systems. J Chem Phys. 1993; 98:10089–10092.

48. Parrinello M, Rahman A. Polymorphic Transitions in Single-Crystals - a New Molecular-Dynamics Method. J Appl Phys. 1981; 52:7182–7190.

49. Hess B, Bekker H, Berendsen HJC, Fraaije JGEM. LINCS: A linear constraint solver for molecular simulations. Journal of Computational Chemistry. 1997; 18:1463–1472.

50. Humphrey W, Dalke A, Schulten K. VMD: Visual molecular dynamics. J Mol Graph Model. 1996; 14:33–38.

51. Zhou Y, Ramachandran S, Oh-Hora M, Rao A, Hogan PG. Pore architecture of the ORAI1 store-operated calcium channel. Proc Natl Acad Sci U S A. 2010; 107:4896–4901. [PubMed: 20194792]

52. Gwack Y, Srikanth S, Feske S, Cruz-Guilloty F, Oh-hora M, Neems DS, Hogan PG, Rao A. Biochemical and functional characterization of Orai proteins. J Biol Chem. 2007; 282:16232–16243. [PubMed: 17293345]

53. Zhou Y, Meraner P, Kwon HT, Machnes D, Oh-hora M, Zimmer J, Huang Y, Stura A, Rao A, Hogan PG. STIM1 gates the store-operated calcium channel ORAI1 in vitro. Nat Struct Mol Biol. 2010; 17:112–116. [PubMed: 20037597]

54. Grynkiewicz G, Poenie M, Tsien RY. A new generation of Ca2+ indicators with greatly improved fluorescence properties. J Biol Chem. 1985; 260:3440–3450. [PubMed: 3838314]

Europe PMC Funders Author Manuscripts

One-sentence summary

A special region of the store-operated calcium channel maintains channel function under conditions of low extracellular calcium.

Europe PMC Funders Author Manuscripts

Editor's Summary

Enhancing Ca^{2+} concentration at the pore

Store-operated calcium entry (SOCE) produces local calcium signals that not only refill intracellular calcium stores, but also regulate specific downstream signaling events, such as activation of the calcium-dependent transcription factor NFAT. The channel complexes that mediate the calcium influx include the calcium-sensing proteins of the STIM family and the pore-forming subunits of the Orai family. These channels must function in cells that are part of tissues, as well as cells that circulate in the blood stream; thus cells that are exposed to very different concentrations of extracellular calcium. Using molecular dynamics simulations and analysis of mutant proteins in cells, Frischauf *et al.* identified a region, the calcium-accumulating region (CAR), in Orai1 that enhanced the local concentration of calcium at the entrance to the pore. The importance of CAR was most evident under conditions of low extracellular calcium, as would occur in cells of the skin. NFAT activity was impaired in cells expressing STIM1 and Orai channel proteins with mutations in CAR or that disrupted CAR function. Thus, CAR enables Orai to mediate SOCE-induced calcium signaling even under diverse extracellular calcium concentrations.

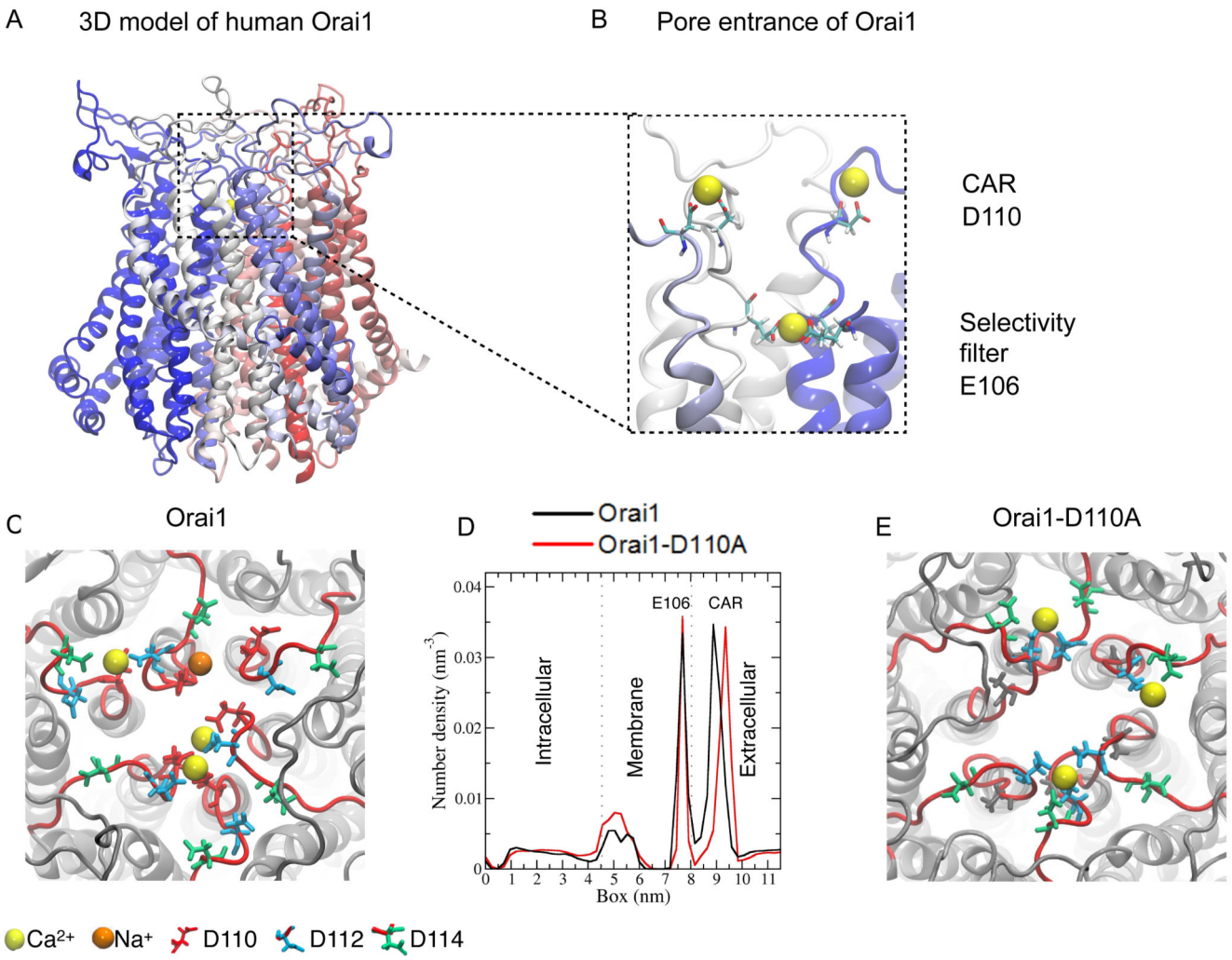

Figure 1. Molecular dynamics simulations identifies CAR in extracellular loop1 of human Orai1.

(A) Atomic 3D model of human Orai1 (E62 – G297), including the loop segments that were not present in the *Drosophila* Orai crystal structure on which this human Orai1 model is based. The panel shows a side view of a modelled hexameric structure with each monomer individually colored. **(B)** Side view of a representative snapshot of a molecular dynamics simulation of the Orai1 pore showing Ca^{2+} binding (yellow balls) to the selectivity filter (Glu^{106} sidechain shown) and the loop1 segments (Asp^{110} sidechain shown). **(C and E)** Top view of a representative snapshot of a molecular dynamics simulation of Orai1 and Orai1-D110A simulation. **(D)** One-dimensional density number of ion concentration through the Orai1 channel (black) and Orai1-D110A (red) from the intracellular to the extracellular side (in Z-direction). The dotted lines mark the membrane headgroup regions and the peak between 7 and 8 nm corresponds to the selectivity filter.

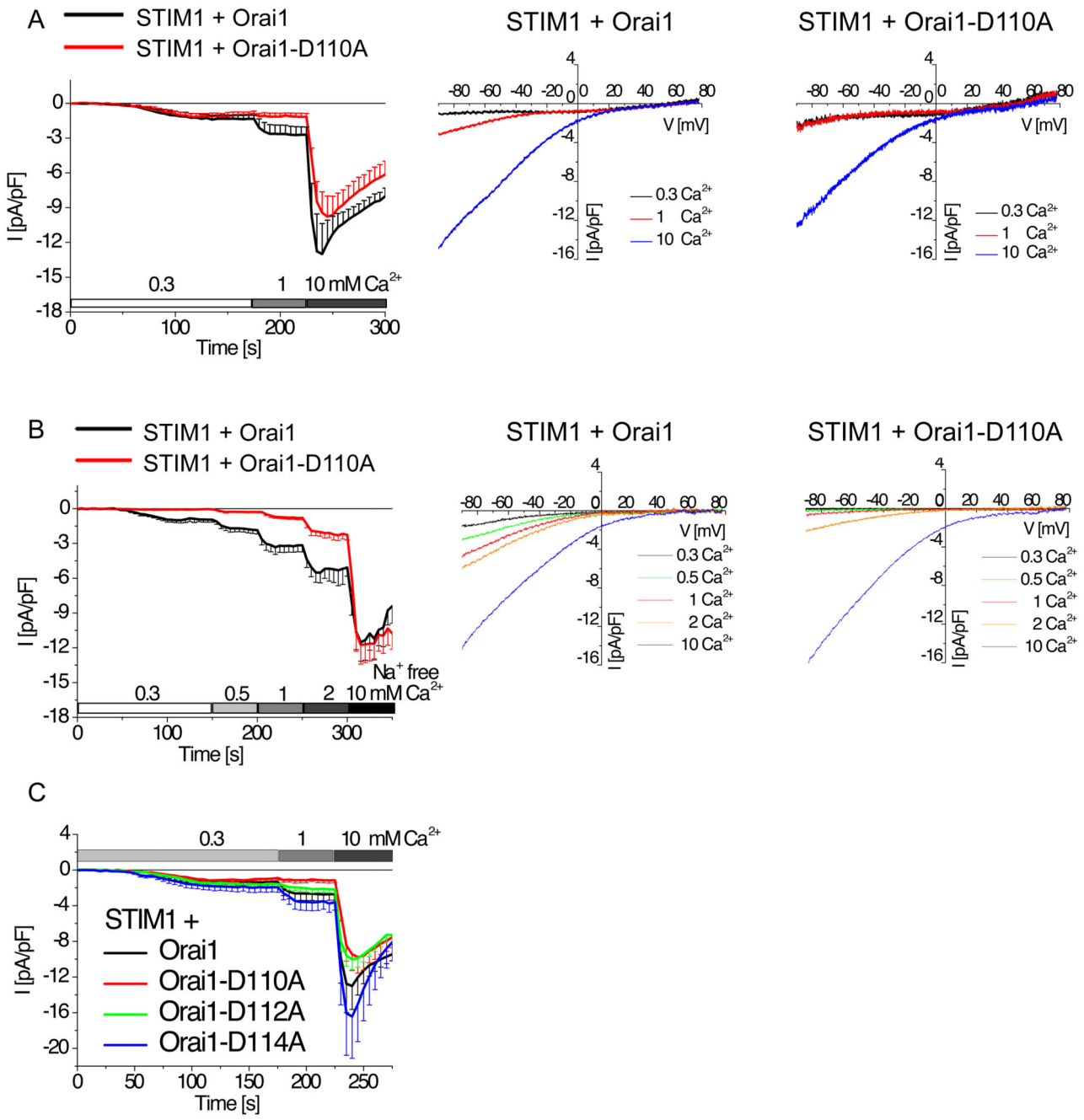

Figure 2. CAR promotes Ca^{2+} permeation through the Orai1 channel.

(A) Whole-cell patch-clamp experiments show time course of currents mediated by mCherry-tagged STIM1 coexpressed with wild-type or mutant eYFP-tagged Orai1 as indicated in HEK 293 cells (n = 9 -10). Currents were only measured for cells positive for mCherry-tagged STIM1 and wild-type or mutant eYFP-tagged Orai1. Current activation by endoplasmic reticulum store-depletion was mediated by 20 mM EGTA in the patch pipette and stepwise current increases were recorded at 0.3 mM, 1 mM and 10 mM Ca^{2+} concentration with Na^+-containing (A, C) or Na^+-free (B) solution. Representative current-

Europe PMC Funders Author Manuscripts

Europe PMC Funders Author Manuscripts

voltage relationship with properties of Ca^{2+}-selective currents are shown for wt-Orai1 and Orai1-D110A (A,B). **(B)** Whole-cell patch-clamp experiments show time course of currents mediated mCherry-tagged STIM1 coexpressed with wild-type or mutant eYFP-tagged Orai1 as indicated in HEK 293 cells (n = 7 – 10). Store depletion was achieved and currents were recorded as in (A) with increasing Ca^{2+} concentrations in a Na^{+}-free solution. Orai1 and Orai1-D110A maximum currents at various extracellular Ca^{2+} concentrations were compared for statistical significance by t-test. In a Na^{+}-containing solution (A), currents are significantly different ($p < 0.05$) in a 1 mM Ca^{2+} solution. In a Na^{+}-free extracellular solution (B) currents were significantly different ($p < 0.05$) in a 0.3, 0.5, 1, and 2 mM Ca^{2+} solution. **(C)** Similar time-course for indicated mutants as in (A,B). Currents of Orai1-D112A or Orai1-D114A were compared by t-test for significance and are not significantly different to those of wild-type Orai1.

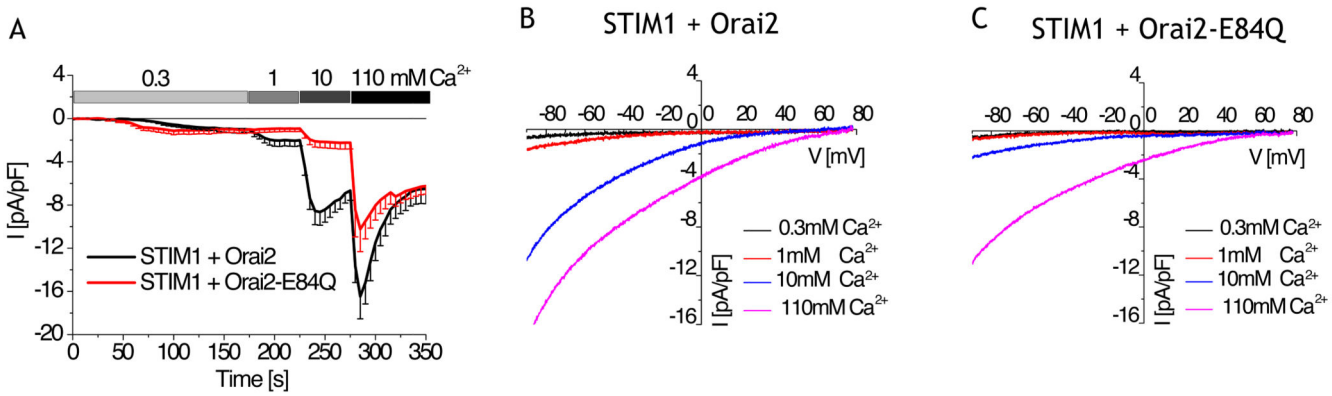

Figure 3. CAR promotes Ca^{2+} permeation through the Orai2 channel.

(A) Whole-cell patch-clamp experiments show time course of currents mediated mCherry-tagged STIM1 coexpressed with wild-type or mutant eYFP-tagged Orai2 as indicated in HEK cells exposed to 20 mM EGTA in the patch pipette and then stepwise increase in Ca^{2+} concentration with Na^{+}-containing solution (n = 8 – 9). Wild-type Orai2 and mutant Orai2 were analyzed by t-test for statistical significance for their maximum currents at various extracellular Ca^{2+} concentrations. Their currents are significantly different ($p < 0.05$) in a 1, 10, and 110 mM Ca^{2+} solution. **(B, C)** Representative current-voltage relationship of Orai2- or Orai2-E84Q-mediated SOCE currents for experiments shown in (A).

Europe PMC Funders Author Manuscripts

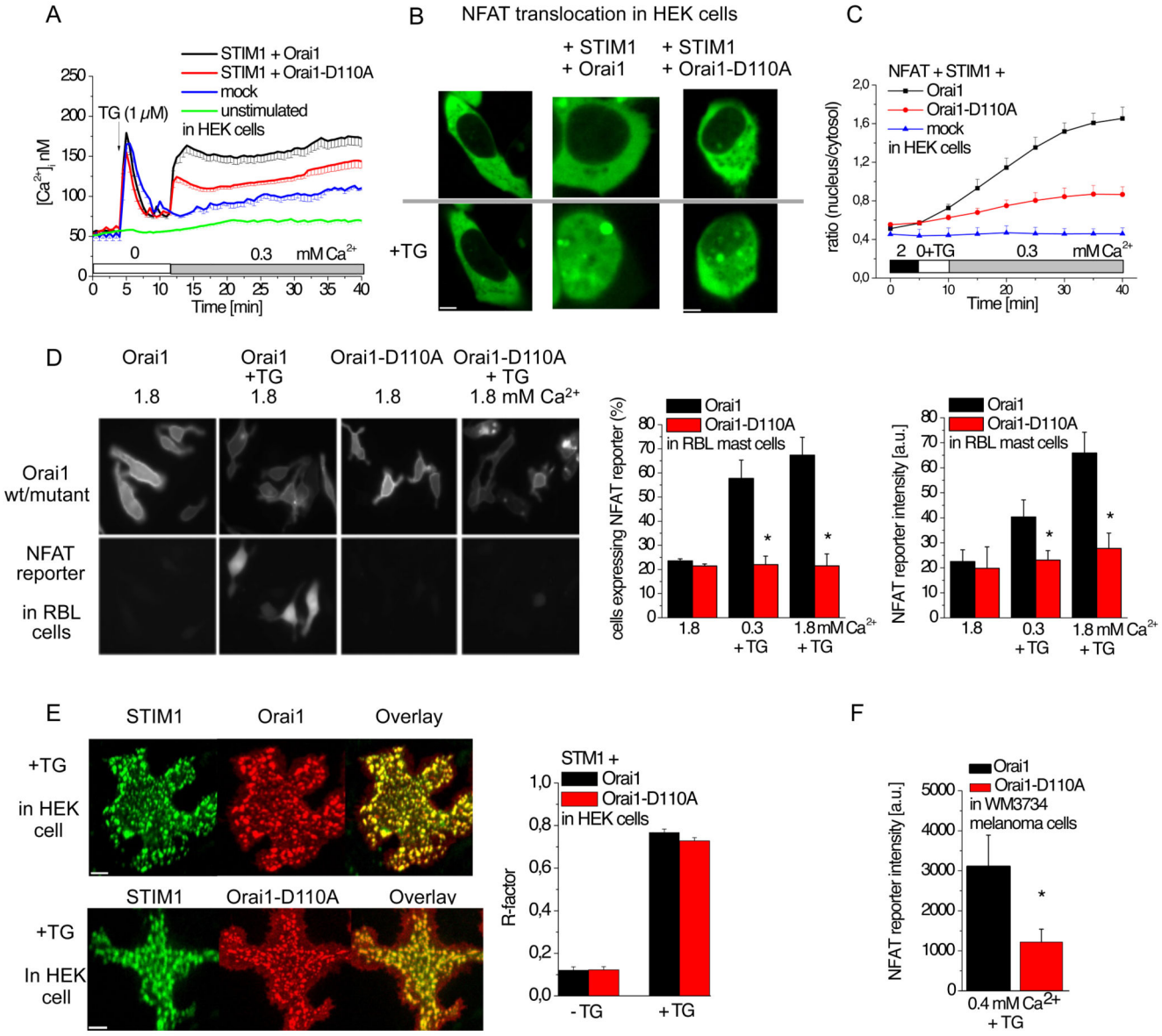

Figure 4. Activation of the Orai1 CAR mutant results in decreased SOCE-induced cytosolic Ca^{2+} concentrations and NFAT signaling.

(A) Time course of cytosolic Ca^{2+} concentration measured by Fura-2 microscopy for HEK 293 cells coexpressing mCherry-tagged STIM1 and eYFP-tagged wild-type or mutant Orai1, or mock-transfected cells, or and unstimulated cells that were not exposed to thapsigargin (TG). In Ca^{2+}-free extracellular solution, ER stores were depleted with thapsigargin (TG) at 3 min and 0.3 mM Ca^{2+} was added at 12 min (n = 12 - 25). STIM + Orai1 data were compared to STI + Orai-D110A at XX by t-test and determined significantly different ($p < 0.05$) upon addition of extracellular Ca^{2+}. **(B)** Representative images of GFP-NFAT localization in mock-transfected HEK cells or HEK cells coexpressing Cherry-tagged STIM1 and the indicated eYFP-tagged Orai1 before (upper panel) or 30 minutes after exposure to 1 μM TG (lower panel) in a 0.3 mM Ca^{2+}-containing bath solution. **(C)** Time

course showing the ratio of nucleus to cytosolic GFP-NFAT fluorescence intensity for cells coexpressing GFP-NFAT with the indicated transfected proteins. ER store depletion was induced by 1 μM TG at 5 minutes in a Ca^{2+}-free solution and 0.3 mM Ca^{2+} was added at 10 minutes (n = 5 – 12). The ratios for NFAT + STIM1 + Orai1 were compared to those for NFAT + STIM1 + Orai1-D110A using a t-test at XX and determined significantly different ($p < 0.05$) in a 0.3 mM Ca^{2+} solution **(D)** Shown are quantitative analysis and representative images of activation of an NFAT-controlled reporter gene (NFAT reporter) in RBL mast cells expressing RFP under the control of an NFAT-regulated promoter, CFP-tagged STIM1, and eYFP-tagged wild-type or mutant Orai1 that were exposed to 100 nM TG for 3.5 hours in 0.3 mM or 1.8 mM Ca^{2+}-containing medium. Representative images are shown on the left, the percent of cells positive for RFP fluorescence are shown in the middle (n = 34 – 86 cells), and the intensity of RFP fluorescence is shown on the right (n = 34 – 86 cells). Data were analyzed by t-test for statistical significance ($p < 0.05$) as indicated by the stars. (**E**) Representative HEK 293 cells show CFP-tagged STIM1 cluster formation with eYFP-tagged Orai1 or eYFP-tagged Orai1-D110A upon store depletion with 1 μM TG and presence of 2mM Ca^{2+} solution. R-factor as a measure of the linear correlation between STIM1 and Orai1, as well as STIM1 and Orai1-D110A before and after store depletion by TG (n = 28 – 39). **(F)** The NFAT reporter gene, CFP-tagged STIM1 and eYFP-tagged Orai1 or eYFP-tagged Orai1-D110A coexpressed in WM3734 melanoma cells were treated with 100 nM thapsigargin for one hour in a 0.4 mM Ca^{2+}-containing media. Intensity of NFAT driven RFP expression was determined in those cells that exhibited STIM1 and Orai1 or Orai1-D110A expression 24h hours after thapsigargin treatment. Data were analyzed by t-test for statistical significance ($p < 0.05$) and determined that Orai1-D110A intensity is significantly decreased compared to wild-type Orai1.

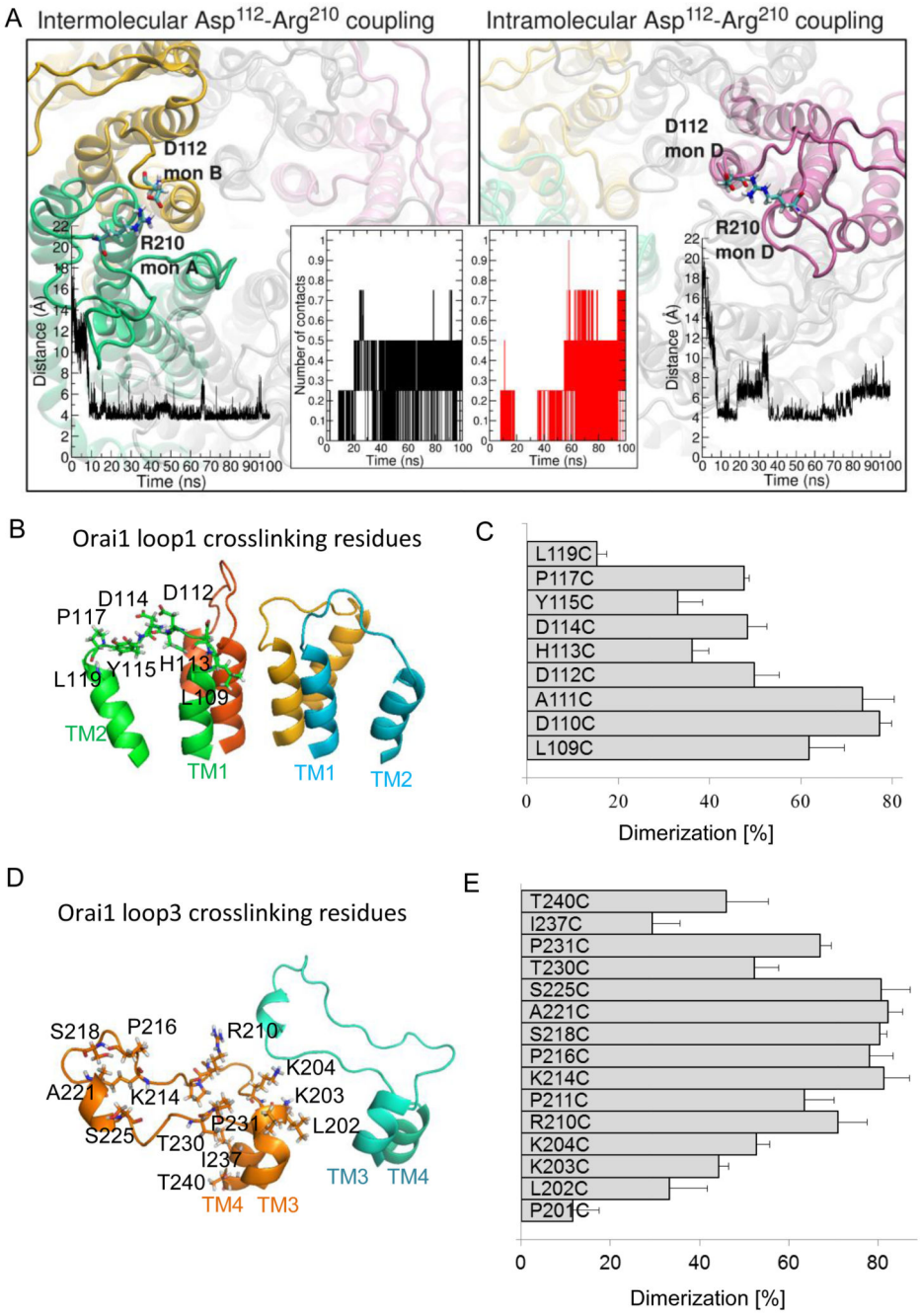

Figure 5. Loop3 residues form electrostatic interactions with CAR in Orai1

(A) Representative snapshot of the intermolecular (left panel) and intramolecular (right panel) electrostatic interaction of Arg^{210} with Asp^{112} predicted by molecular dynamics simulation. Potential Asp^{112}-Arg^{210} contacts were counted based on a distance ≤ 4.5 Å between the carboxyl carbon of loop1 aspartic acid and the guanidino carbon of loop3 arginine as shown in the time-courses (left inset graph for intermolecular interaction, and right inset graph for intramolecular interaction). The time-dependent number of intramolecular and intermolecular contacts between Asp^{112} in loop1 and Arg^{210} in loop3 for

a single Orai1 channel within 100 ns is shown in the central inset. (**B**) Selected single cysteine mutants in Orai1 loop1 (L109C, D110C, A111C, D112C, H113C, D114C, P117C, L110C) are shown as sticks in a 3D homology model of Orai1. (**C**) Percentage of dimerization for cysteine mutants upon CuP treatment were calculated. Data are shown as the average + SEM (n = 4 -8). (**D**) Structural modelling of the loop3 domain in Orai1 yielded a random coil region, highlighting the residues (P201, L202, K203, K204, R210, P211, K214, P216, S218, A221, S225, T230, P231, I237, T240), which were individually engineered to cysteines. (**E**) Percentage of dimerization for cysteine mutants upon CuP treatment were calculated. Data are shown as the average + SEM (n = 4 – 8).

Europe PMC Funders Author Manuscripts

Europe PMC Funders Author Manuscripts

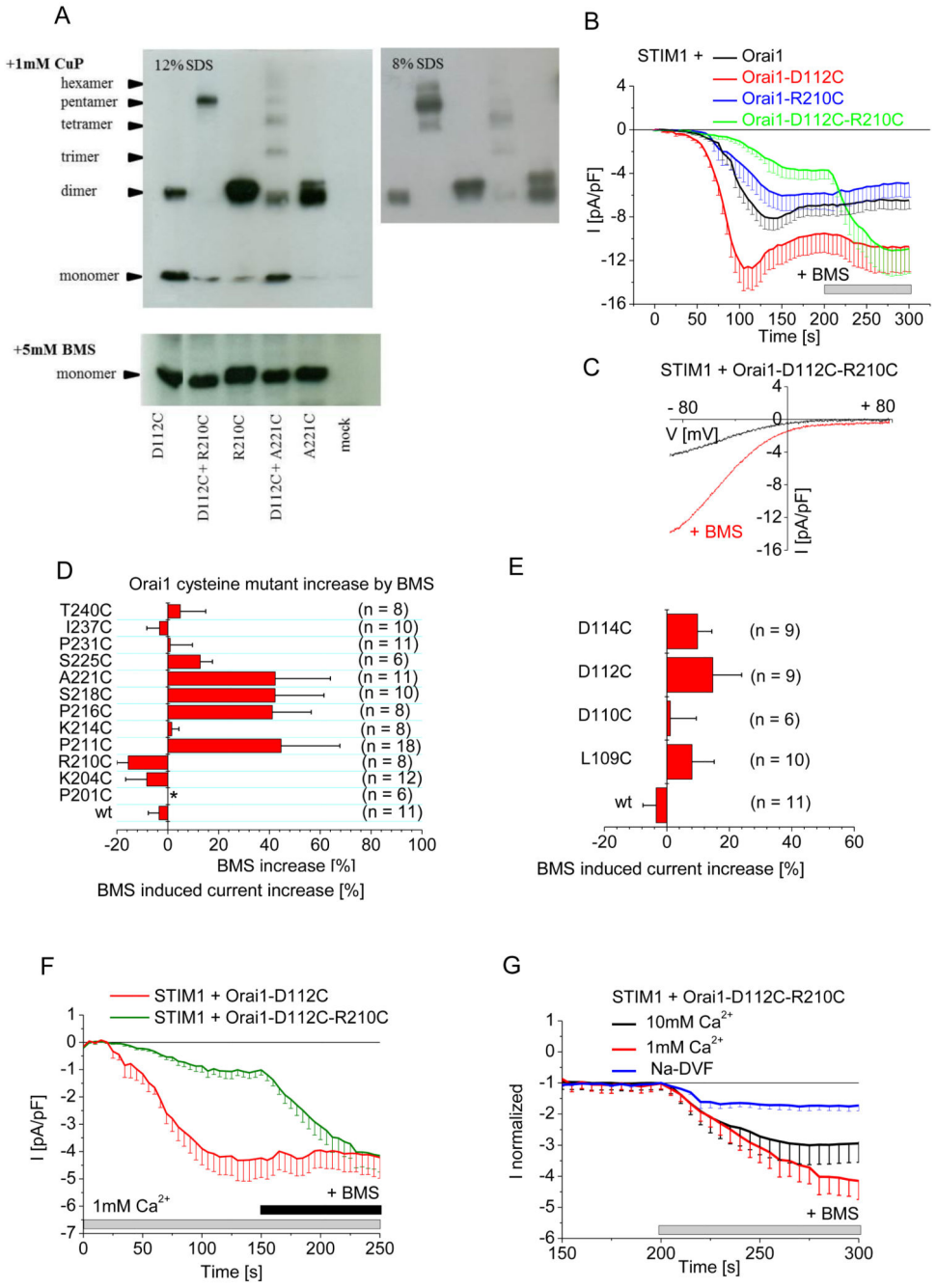

Figure 6. Disruption of CAR through forced dimerization between loop1 and loop3 inhibits SOCE.

(A) Oligomerization of the indicated Orai1 single and double cysteine mutants overexpressed in HEK 293 cells were detected by SDS PAGE (12%, left; 8% right) after incubation with 1mM CuP (upper panel) or after the addition of 5 mM BMS (lower panel). **(B)** Whole-cell patch-clamp experiments show time course of currents mediated by Cherry-tagged STIM1 coexpressed with wild-type eYFP-tagged Orai1 or Orai1 mutant as indicated in HEK cells exposed to 20 mM EGTA in the patch pipette and a 10 mM Ca^{2+}-containing

Europe PMC Funders Author Manuscripts

solution, and upon maximum current activation, BMS (5 mM) was added (n = 8 - 11). Analysis by t-test, with $p < 0.05$ for statistical significance, indicated that Orai1-D112C maximum currents are significantly different from those of Orai1-D112C-R210C in the absence but not in the presence of BMS. **(C)** Current-voltage relationship of the store-operated activation of Orai1-D112C-R210C and upon BMS stimulation from a representative experiment from (B). (**D**) The BMS-dependent increase in currents mediated by wild-type (wt) eYFP-tagged Orai1 and the indicated eYFP-tagged loop3 cysteine mutants upon maximum store-dependent activation. All Orai1 mutants, except P201C, yielded a store-dependent current when coexpressed with STIM1 in HEK 293 cells exposed to 20 mM EGTA in the patch pipette and a 10 mM Ca^{2+}-containing solution. Data are shown as the mean + SEM. (**E**) The BMS-dependent increase in currents mediated by wild-type (wt) eYFP-tagged Orai1 and the indicated YFP-tagged loop1 cysteine mutants upon maximum store-dependent activation under the same conditions as in (D). **(F)** Whole-cell patch-clamp experiments show time course of currents mediated by Cherry-tagged STIM1 coexpressed with wild-type eYFP-tagged Orai1 or Orai1 mutant in a 1mM Ca^{2+} containing bath solution (n= 7-11 cells). Maximum currents of Orai1-D112C and Orai1-D112C-R210C were analyzed by t-test before and after addition of BMS for statistical significance, and are significantly different ($p < 0.05$) before addition of BMS. (**G**) Comparison of relative BMS-dependent stimulation in currents mediated by Cherry-tagged STIM1 and eYFP-tagged Orai1-D112C-R210C coexpressed in HEK 293 cells in the presence of the indicated extracellular solutions (n = 6 - 11). Data were analyzed by t-test for statistical significance ($p < 0.05$) of maximum currents upon BMS treatment, determining that 1mM and 10mM Ca^{2+} currents are significantly different compared to sodium based currents.

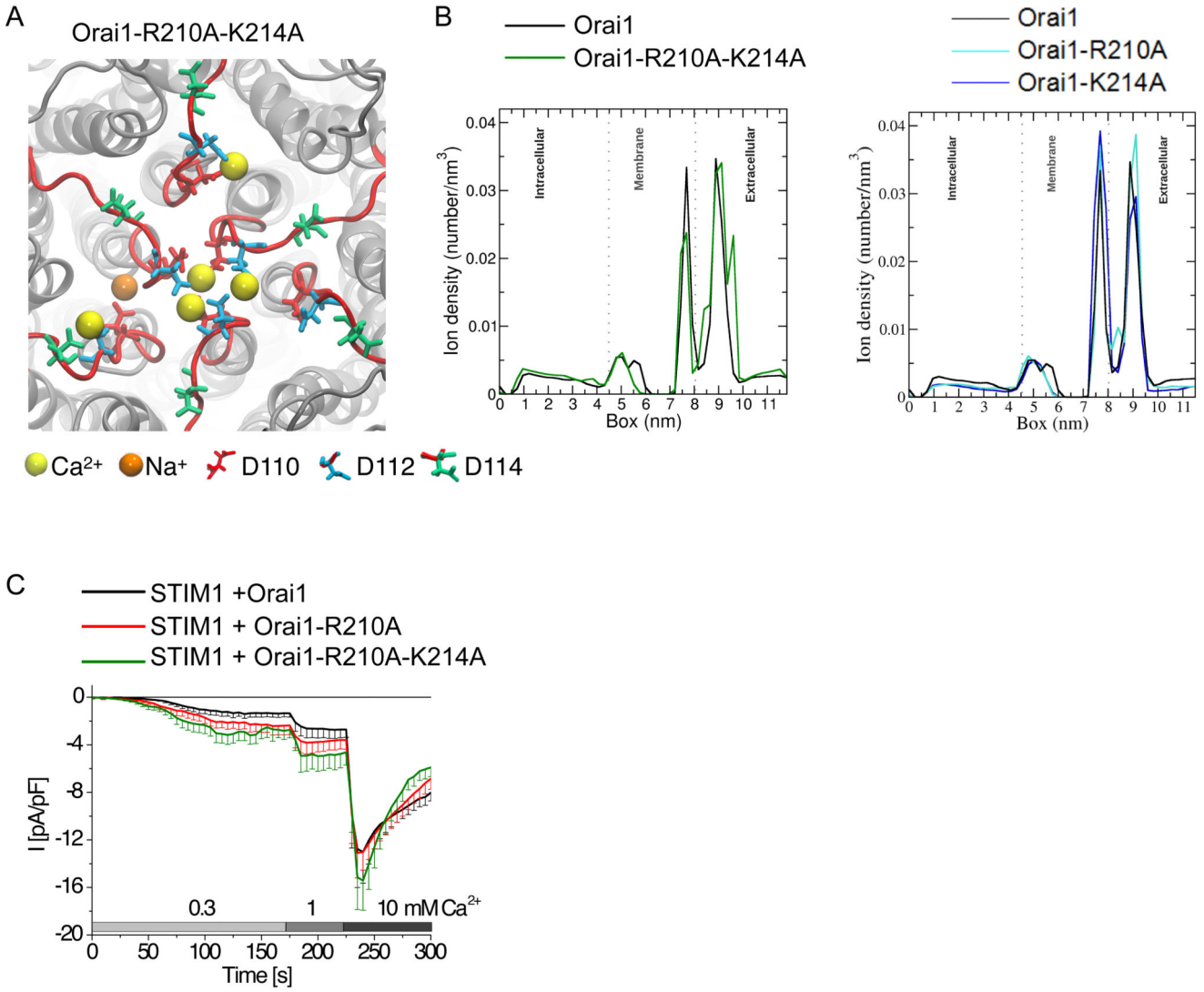

Figure 7. Ca^{2+} and loop3 compete for binding to CAR.

(A) Top view of a representative snapshot of the molecular dynamics simulation of Orai1-R210A-K214A. Ca^{2+} ions are represented as yellow balls, Na^{+} as orange balls. **(B)** One-dimensional density number of ion concentration through the Orai1 channel (black) and the double mutant (left) or the single mutants (right) from the intracellular to the extracellular side (in Z-direction). Dotted lines mark the membrane head group regions and the peak between 7 and 8 nm corresponds to the selectivity filter. **(C)** Whole-cell patch-clamp experiments show time course of currents mediated by Cherry-tagged STIM1 and YFP-tagged wild-type or mutant Orai1 expressed in HEK 293 cells exposed to 20 mM EGTA in the patch pipette and then exposed to the indicated Ca^{2+} solutions (n = 10 – 14). Maximum currents were analyzed by t-test for statistical significance; Orai1 and Orai1-R210A-K214A are significantly different ($p < 0.05$) in a 0.3 mM and 1 mM Ca^{2+} solution. Orai1 and Orai1-R210A maximum currents are significantly different in a 0.3 mM Ca^{2+} solution.